# The geometry and the number of contacts of monodisperse sphere packs using X-Ray tomography

M. Saadatfar, A. Kabla, T. J. Senden, T. Aste

*Department of Applied Mathematics, Research School of Physical Sciences and Engineering,*
The Australian National University, Canberra ACT 0200, Australia

The three-dimensional structure of very large samples of monodisperse bead packs is studied by means of X-Ray Computed Tomography. We retrieve the coordinates of each bead in the pack and we calculate the average coordination number by using the tomographic images to single out the neighbors in contact. The results are compared with the average coordination number obtained in (Aste et al. 2005) by using a deconvolution technique. We show that the coordination number increases with the packing fraction, varying between $6.9$ and $8.2$ for packing fractions between $0.59$ and $0.64$.

## 1 INTRODUCTION

The science of granular matter has a long history, with the classic contributions from Faraday (on *pattern* formation in granular materials) and Reynolds (on the *dilatancy* phenomenon). More recently the topic has attracted condensed matter physicists (Jaeger et al. 1996) and scientists studying complex systems (Bak et al. 1987), who have sought to study granular materials as models for more complex materials and phenomena. As such, granular materials have been typically studied either at the structural level (grain scale), or as a continuous medium to observe bulk properties. The goal has always been to bridge these two views, to explain the relationships between structure and property.

In order to fully understand and characterize granular packing at either scale we need to extract their structure accurately. To this end, one would aim to detail shape, position and contacts of all grains in a pack. However, to attain such detail, with precision, on populations of grains sufficient to observe bulk properties presents a considerable technical challenge. Such a challenge, was first undertaken by (Bernal 1959) and (Scott 1962) who measured the geometrical structure of grain packs and calculate their coordination numbers. They analyzed the simplest granular pack consisting of monosized spheres which can model realistic systems such as powders (Cumberland and Crawford 1987). Although Scott and Bernal pioneered this field, their manual grain-by-grain approach was limited to small populations $(< 1000)$ and was ultimately restrictive. In recent years, X-ray tomography has been used to analyze the packing structure at grain scale (Seidler et al. 2000; Sederman et al. 2001; Richard et al. 2003). However, these first studies were limited by rather low resolutions and small sample sizes. Such limitations were overtaken in (Aste et al. 2004; Aste et al. 2005) where a detailed analysis of very large samples (up to 140,000 beads) was performed with unprecedented accuracy disclosing the properties of the geometrical organization in monosized sphere packs.

In this paper, we present the details of the X-ray CT apparatus and image acquisition technique we employed to acquire the tomograms of the samples studied in (Aste et al. 2004; Aste et al. 2005); we describe the technique used to detect the sphere centers; and we present a novel method to calculate the coordination number.

## 2 EXPERIMENTAL APPARATUS

### 2.1 Image acquisition

Tomography is a technique that generates a data set, a tomogram, which gives a three-dimensional representation of the structure and variation of composition within a specimen. We used an X-ray tomography apparatus where both the X-ray source and detector are optimized for high resolution and for maximal field of view (Sakellariou et al. 2004; Sakellariou et al. 2004). Such experimental apparatus has a cone beam geometry which allow magnifications between $\times 1.1$ to over $\times 100$ by moving the position of the rotation stage and the camera. The limiting resolution is determined by the X-ray source and it is around 2-5 microns, depending on operating voltage (30-120 kV). The camera can acquire radiographs with $2048^2$

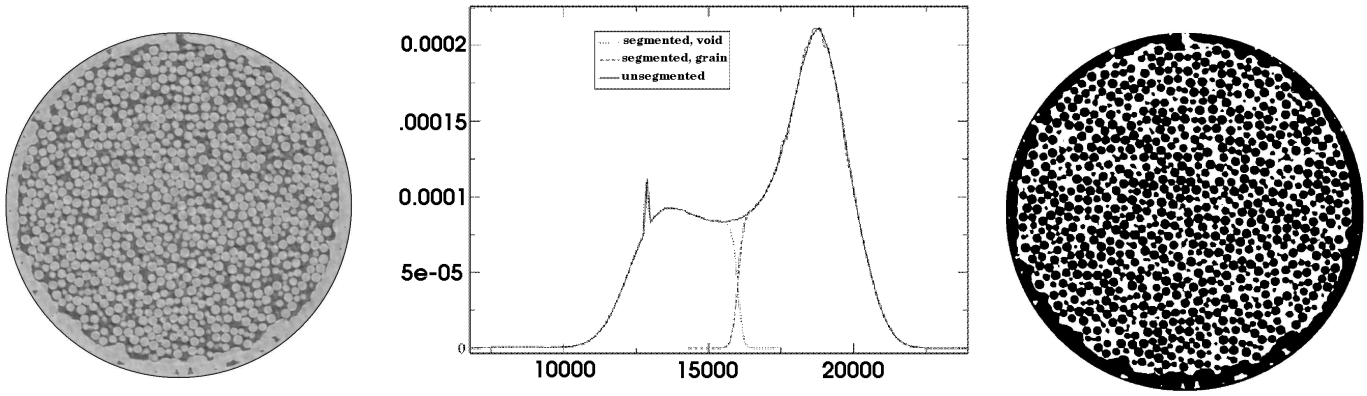


(a) (b) (c)

Figure 1: (a) Grey-scale X-ray density map of a slice of Sample C . (b) Density histogram for the full image volume of Sample C , and (c) the same slice after phase separation into pore and solid phases.

pixels at a depth of $16$ bits per pixel. The specimen rotation stage has an angular accuracy of $0.001°$. The large dynamic range of the X-ray camera is ideal for the discrimination of fine features in complex materials. Filters are frequently used to minimize beam hardening artifacts due to the polychromatic nature of the source.

By using this experimental apparatus, we acquire three dimensional image of $6$ samples: two large bead packs (samples A and C), each containing over $10^5$, with a resolution of $0.05\ mm$, and a tomogram size of $2048^3$ voxels; and four smaller samples (B, D, E, F) with resolutions of $0.06\ mm$, and tomogram size of $1024^3$ voxels. The beads used in the experiments are made of polymethylmethacrylate at two different sizes. Samples A and C are comprised of beads with diameter $1$ mm and samples B, D, E, and F are made up of beads with diameter $1.6$ mm. These are the same samples studied in (Aste et al. 2005). The number of spheres in the central region in which we perform the analysis ($N$) and the fraction of volume occupied by the spheres (density) are reported in Table 1).

### 2.2 Reconstructed X-ray density map and material phase identification

Fig. 1(a)(c) show an example of X-ray density maps and the histogram (Fig. 1(b)) for a slice within a tomogram of sample C. The tomographic image consists of a cubic array of unscaled density values, each corresponding to a finite volume cube (voxel) of the sample. An immediate goal is to differentiate the attenuation map into distinct pore and solid (grain) phases.

The density histogram (Fig. 1(b)) shows two distinct peaks associated with the two phases. The peak centered around $19500$ is associated with the granule phase. The lower peak around $13000$ is associated with the void phase. To distinguish between the two phases, it is sufficient to apply a simple threshold (at $16000$) followed by the removal of isolated solid clusters to eliminate noise artifacts. A comparison between the grey-scale (density map) and binarised (segmented) image of a slice of Sample C is shown in Fig. 1(a) and (c).

| | density | $N$ | $n_c$ |
|---|---|---|---|
| A | $0.586 \pm 0.005$ | 108,696 | **6.88** |
| B | $0.596 \pm 0.006$ | 27,490 | **7.05** |
| C | $0.619 \pm 0.005$ | 138,696 | **7.79** |
| D | $0.626 \pm 0.008$ | 29,134 | **7.66** |
| E | $0.630 \pm 0.01$ | 29,438 | **8.16** |
| F | $0.640 \pm 0.005$ | 29,892 | **8.19** |

Table 1: Sample density and their interval of variations ($\pm$) within each sample (Aste et al. 2005); number of spheres in the central region in which we perform the analysis ($N$); average number of neighbors in contact ($n_c$).

## 3 ANALYSIS

### 3.1 Determining the centers of beads

Let us consider a tomographic image with $V$ voxels. In order to separate individual beads within the packing, we employ a convolution method which moves a reference sphere with a radius smaller than the beads and finds the overlap between the reference sphere $S(\vec{r})$ and the (segmented) bead pack $P(\vec{r})$. The convolution of $P$ and $S$ is:

$$I(\vec{r}_j) = \sum_{i=1}^{V} S(\vec{r}_j - \vec{r}_i) \cdot P(\vec{r}_i) \qquad (1)$$

The above convolution can be implemented very efficiently by applying the convolution theorem which allows to transform the convolution into a product in Fourier space.

$$\mathcal{F}[I] = \tilde{I}(\vec{\kappa}) = \mathcal{F}[S] \cdot \mathcal{F}[P] \qquad (2)$$

where $\mathcal{F}$ represents the (fast) Fourier transform. The inverse Fourier transform of Eq. 2 results in the beads' *Image function*, as expressed in Eq. 1:

$$I = \mathcal{F}^{-1}[\tilde{I}(\vec{\kappa})] \qquad (3)$$

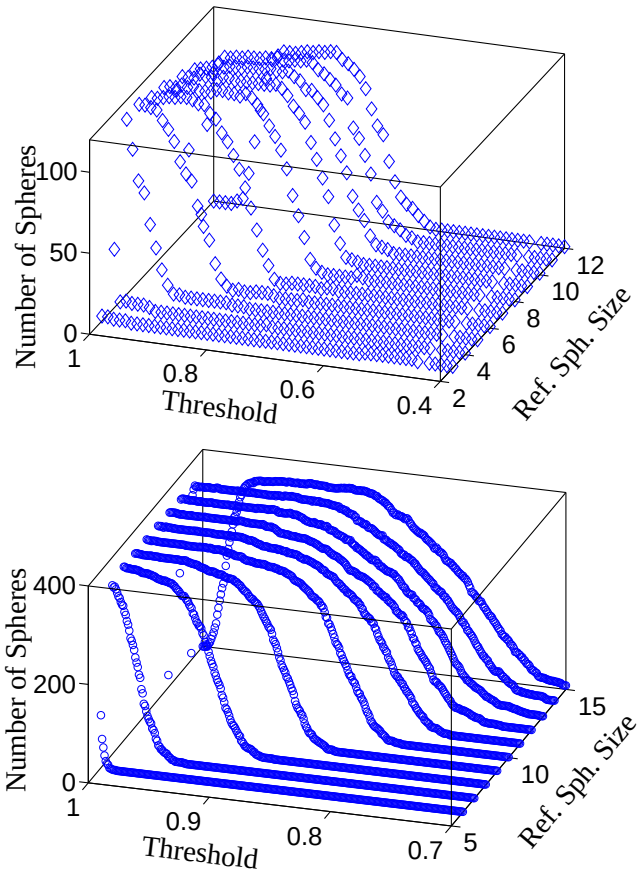


Figure 2: Number of spheres detected versus intensity threshold and reference sphere size. The above plot was obtained in a $200^3$ subvolume of two different classes of sphere packs (top) Sample F and Sample A (bottom).

The result of Eq. 3 is an intensity map of the overlap between the reference sphere and the beads, where the voxels closer to the sphere centers have higher intensities (in fact the peaks of the highest intensity represent the group of voxels around sphere centers in the original image). A threshold on the intensity map locates the groups of voxels surrounding the sphere centers. The center of each sphere is then computed as the center of mass of each cluster weighted by the intensity of each voxel:

$$\vec{R}_{cm} = \frac{\sum_i \vec{r}_i I(\vec{r}_i)}{\sum_i I(\vec{r}_i)} \qquad (4)$$

where $i$ runs over the group of voxels in each cluster and $I$ is the intensity information held by that voxel. Below we will investigate the values of the threshold and the reference sphere size which give optimal estimates for the sphere centers' positions.

### 3.2 Reference sphere size and intensity threshold

The precision in which the sphere centers' position is calculated depends on the spacial resolution of the tomograms and also on the size of the cluster surrounding the sphere centers after thresholding the *Image function* as described in Section 3.1. The spatial resolutions of the tomograms are between one and two voxels. Therefore the precision on the center of mass of a cluster of $\nu$ voxels will be within $1/\nu$ to $2/\nu$. This suggests that, in order to minimize the error on the centers, we need to optimally choose the two parameters discussed in the previous section (i.e. reference sphere size and intensity threshold), so that $\nu$ will be as large as possible. We have searched for the optimal choice of the parameters by varying these two quantities and computing the resulting number of spheres detected in a given portion of the sample. In Fig. 2 the number of detected spheres is reported as a function of the reference sphere size and the threshold. As shown in the plot, there is a rather large region in which the same number of spheres are detected. This plateau indicates the region in which the two parameters can be chosen from.
We chose the threshold value at $0.95$ for samples A, C, E and at $0.93$ for samples B, D, F, and we fixed the reference sphere radius at $13$ for sample A, C, and at $11$ for sample E, and at $10$ for samples B, D, F. A cluster size of $80$ voxels (samples B, D, E, F) and $400$ voxels (samples A, C) are obtained, which implies precisions on the sphere centers within $3$ % and $0.5$ % of the voxel sizes, respectively.

Once the correct parameters have been chosen and the sphere centers are calculated, we can reconstruct the bead packs based on the information on the bead radii and their centers. In Fig. 3 a reconstructed bead pack (sample C) is displayed.

### 3.3 Number of neighbors in contact

One of the most interesting parameters which has been widely investigated in the literature of granular packs is the average number of spheres in contact with each sphere (Bernal 1959; Scott 1962; Mason 1968). An exact computation of the number of touching spheres can only be deduced from the geometry of granular packs with infinite resolution where the contact points can be identified with infinite precision. In (Aste et al. 2005) a deconvolution method, based on the radial distance between the bead centers, was devised to find the average number of touching neighbors to each sphere.

In this paper we use the information about the lo-

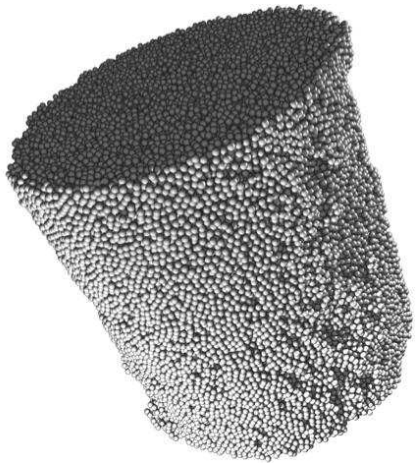

Figure 3: A reconstructed pack from the coordinates of the sphere centers.

cation of sphere centers and the segmented image of granular packs directly to determine the average coordination number of each bead in the pack. This method is less sensitive to the center precision and polydisperisity than the deconvolution method presented in (Aste et al. 2005), and it has the advantage of giving local information about the coordination number of each bead in the pack. However, its precision is limited by the voxel resolution.

By drawing a box of certain size between the centers of neighboring beads, we can determine whether two beads are in contact or not by distinguishing between boxes which contain one or two clusters (Fig. 4). The result of this analysis is reported in Table 1. This method, of course, depends highly on the resolution of the the tomogram. Since the resolution of the samples studied in this paper is between $1$ to $2$ voxels, we expect to detect neighbors within radial distances of 1 or 2 voxels larger than the sphere-diameter. A comparison between the data in Table.1 and the results from the deconvolution method in (Aste et al. 2005) shows a very good agreement between these two techniques. We find that the present method overestimates the number of actual contacts giving results equivalent to those in (Aste et al. 2005) for neighbors within radial distances between 1.05 and 1.07 bead diameters.

## 4 CONCLUSIONS

We have shown that the position of the bead centres in large packings can be retrieved with sub-voxel precision by using a convolution method associated with a thresholding. This method is made numerically efficient by applying the convolution theorem and performing the convolution as a product in Fourier space (Aste et al. 2004; Aste et al. 2005). We computed the average number of beads in contact, distinguishing between touching and non-touching grains, by looking at the tomograph images. A comparison with the results in (Aste et al. 2005) shows that this method overestimates the actual number of contacts. Considering the precision of the present tomographs, this corresponds to include neighbors up to radial distances $5-7$ percent greater than the diameter of the beads. Experiments with larger beads, which can lead to better precisions, are under current investigation.

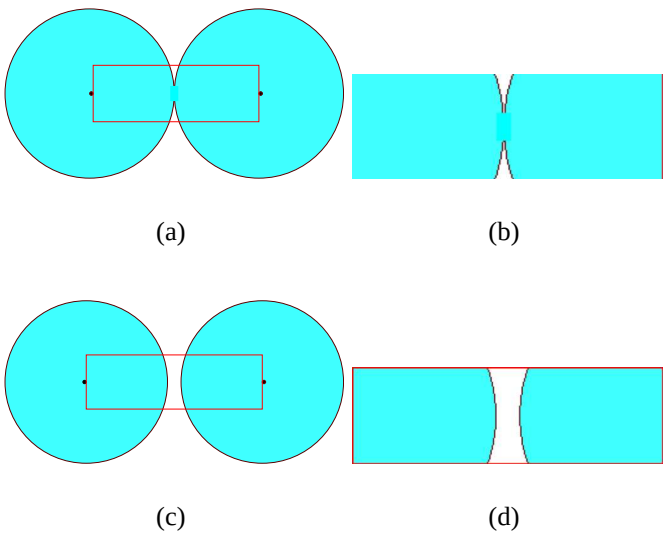


Figure 4: Two dimensional illustration of the method to detect touching spheres. If there are two separate clusters inside a box, the two beads are considered not in contact.

## REFERENCES


Aste, T., M. Saadatfar, and T. J. Senden (2004). Investigating the geometrical structure of disordered sphere packing. *Physica A 339*, 16–23.

Aste, T., M. Saadatfar, and T. J. Senden (2005). *submitted to Physical Review E – cond-mat/0502016*.

Bak, P., C. Tang, and K. Wiesenfeld (1987). Self-organized criticality: An explanation of the 1/f noise. *Phys. Rev. Lett 59*, 381.

Bernal, J. D. (1959). A geometrical approach to the structure of liquids. *Nature 183*, 141.

Cumberland, D. J. and R. J. Crawford (1987). *The Packing of Particles*. Elsevier, Amsterdam.

Jaeger, H. M., S. R. Nagel, and R. P. Behringer (1996). Granular solids, liquids, and gases. *Rev. Mod. Phys. 68*, 1259.

Mason, G. (1968). Radial distribution function from small packings of spheres. *Nature 217*, 733.

Richard, P., P. Philippe, F. Barbe, S. Bourles, X. Thibault, and D. Bideau (2003). Analysis by x-ray microtomography of granular compaction. *Phys. Rev. E 68*, 20301.

Sakellariou, A., T. J. Sawkins, T. J. Senden, and A. Limaye (2004). X-ray tomography for mesoscale physics applications. *Physica A 339*, 152–158.

Sakellariou, A., T. J. Senden, T. J. Sawkins, M. A. Knackstedt, A. Limaye, C. H. Arns, A. P. Sheppard, and R. M. Sok (2004). An x-ray tomography facility for a wide range of mesoscale physics applications. In U. Bonse (Ed.), *Proceedings of SPIE*, Volume 5535, pp. 166–171.

Scott, G. D. (1962). Radial distribution of random close packing of equal spheres. *Nature 194*, 956.

Sederman, A., P. Alexandre, and L. F. Gladden (2001). Structure of packed beds probed by magnetic resonance imaging. *Powder Technology 117*, 255.

Seidler, G. T., G. Martines, L. H. Seeley, K. H. Kim, E. A. Behne, S. Zaranek, S. M. H. B. D. Chapman, and D. L. Brewe (2000).

Granule-by-granule reconstruction of a sand-pile from x-ray microtomography data. *Phys. Rev. E 62*, 8175.